CORA Cork Open Research Archive
Cartlann Taighde Oscailte Chorcaí

Title	Direct and indirect band gaps in Ge under biaxial tensile strain investigated by photoluminescence and photoreflectance studies
Authors	Saladukha, Dzianis;Clavel, M. B.;Murphy-Armando, Felipe;Greene-Diniz, Gabriel;Grüning, M.;Hudait, Mantu;Ochalski, Tomasz J.
Publication date	2018-05-09
Original Citation	Saladukha, D., Clavel, M. B., Murphy-Armando, F., Greene-Diniz, G., Grüning, M., Hudait, M. K. and Ochalski, T. J. (2018) 'Direct and indirect band gaps in Ge under biaxial tensile strain investigated by photoluminescence and photoreflectance studies', Physical Review B, 97(19), 195304 (12 pp). doi: 10.1103/PhysRevB.97.195304
Type of publication	Article (peer-reviewed)
Link to publisher's version	https://link.aps.org/doi/10.1103/PhysRevB.97.195304 - 10.1103/PhysRevB.97.195304
Rights	© 2018 American Physical Society
Download date	2026-11-03 01:57:30
Item downloaded from	https://hdl.handle.net/10468/6238

UCC
University College Cork, Ireland
Coláiste na hOllscoile Corcaigh

Direct and indirect band gaps in Ge under biaxial tensile strain investigated by photoluminescence and photoreflectance studies

D. Saladukha,[1,2] M. B. Clavel,[3] F. Murphy-Armando,[2] G. Greene-Diniz,[4] M. Grüning,[4] M. K. Hudait,[3] and T. J. Ochalski[1,2]

[1]*Centre for Advanced Photonics and Process Analysis, Cork Institute of Technology, Cork T12 P928, Ireland*

[2]*Tyndall National Institute, Lee Maltings, Dyke Parade, Cork T12 R5CP, Ireland*

[3]*Advanced Devices & Sustainable Energy Laboratory (ADSEL), Bradley Department of Electrical and Computer Engineering, Virginia Tech, Blacksburg, Virginia 24061, USA*

[4]*Atomistic Simulation Centre, School of Mathematics and Physics, Queen's University Belfast, University Road, Belfast BT7 1NN, Northern Ireland, United Kingdom*

(Received 15 December 2017; revised manuscript received 9 March 2018; published 9 May 2018)

Germanium is an indirect semiconductor which attracts particular interest as an electronics and photonics material due to low indirect-to-direct band separation. In this work we bend the bands of Ge by means of biaxial tensile strain in order to achieve a direct band gap. Strain is applied by growth of Ge on a lattice mismatched InGaAs buffer layer with variable In content. Band structure is studied by photoluminescence and photoreflectance, giving the indirect and direct bands of the material. Obtained experimental energy band values are compared with a $\mathbf{k}\cdot\mathbf{p}$ simulation. Photoreflectance spectra are also simulated and compared with the experiment. The obtained results indicate direct band structure obtained for a Ge sample with 1.94% strain applied, with preferable Γ valley to heavy hole transition.

DOI: 10.1103/PhysRevB.97.195304

I. INTRODUCTION

In recent years there has been extensive ongoing research in the field of optical interconnects [1–3]. However, an integrated laser-on-a-chip still faces the bottleneck of different substrate materials typically used in current industrial processes for lasers and transistor structures. There are different approaches proposed to combine these substrates such as flip chip [2,4] or wafer bonding [5–7]. Other approaches propose growth of both the laser and transistor structures on a single chip. Some success was reported on InP substrates, [8,9] but the high cost of InP wafers is discouraging for broader applications. Growth of a laser directly on a Si substrate encounters challenges given by the lattice mismatch between common laser materials and Si. However, there are a number of interesting results in this field obtained by growth of a buffer GaAs layer on a Si substrate [10] and by growth of materials with similar lattice parameters, such as GeSn [11–13].

Germanium is a promising material for both photonic and electronic applications. It is an indirect gap semiconductor, but has a direct band valley merely 0.14 eV above the conduction band. This band can be lowered in energy by applying tensile strain to Ge [14,15], turning it into a direct gap semiconductor. This method can also be applied to boost charge carrier mobility [16–18], which has a profound effect on transistor switch rate and is critical for electronic applications. When attempting to increase power density on a chip through miniaturization of the next generation of transistors, heat dissipation becomes challenging in standard metal-oxide-semiconductor field-effect transistors (MOSFETs). Heat is generated not only by transistors, but also by the connection wires. Instead, increasing the transistor switch rate allows keeping the same wiring with an increase of overall processor clock rate. Also, Ge FETs are candidates for low-voltage stage gap transistors [19]. These properties of Ge will provide low energy consumption with easier heat dissipation than existing Si technology. In this paper, we study the band of Ge under biaxial tensile strain, applied by growth of Ge on a lattice mismatched $In_xGa_{1-x}As$ layer, by means of photoluminescence (PL) and photoreflectance (PR) studies. In the beginning we describe the theoretical model of Ge crystal used to calculate energy levels and electron-hole wave-function coupling in the crystal under various strain and temperatures. In the next section we describe growth conditions of the studied samples. This is followed by the experimental methods, PL and PR in particular, including the theory used for spectra interpretation. The main section presents and discusses the results obtained from the experiment and the theoretical modeling, with a short summary in the Conclusions section.

II. THEORETICAL MODEL OF STRAINED Ge

The quantum well energy levels and optical coupling between conduction and valence bands were calculated as follows:

We used the 30-band $\mathbf{k}\cdot\mathbf{p}$ approach that includes the effects of strain from Rideau *et al.* [20], which is based on experiment and *GW* [21] calculations. We added the temperature dependence of the *L* and Γ bands to this model from experiments [22].

The quantum confinement was solved using the envelope approximation numerically, using the $\mathbf{k}\cdot\mathbf{p}$ Hamiltonian mentioned above. The boundary conditions were given by the experimental values of the band gap and effective masses of InGaAs and the calculated band offsets from Ref. [23]. We used the boundary matching conditions from Harrison [24].

 ©2018 American Physical Society

The temperature dependence of the energy gaps in InGaAs is taken from Ref. [25].

The latter approach gives permitted crystal momentum k values for the $\mathbf{k}\cdot\mathbf{p}$ model. The optical coupling constants are extracted from the momentum operator between the wave function of the permitted states in the $\mathbf{k}\cdot\mathbf{p}$ model:

$$\langle\psi_{k_i}|\epsilon\cdot\mathbf{p}|\psi_{k_f}\rangle = \frac{m_0}{\hbar}\langle u_{k_i}|\epsilon\cdot\nabla_{\mathrm{k}}H|u_{k_f}\rangle\int dz\,\phi^*_{k_i}(z)\phi_{k_f}(z), \tag{2.1}$$

where ϕ and u are the envelope and Bloch functions, respectively.

The generation rate of direct band-gap photons goes as

$$R_{\mathrm{dir}} = \frac{2\pi}{\hbar}\left|\langle\psi_{k_i}|\epsilon\cdot\mathbf{p}|\psi_{k_f}\rangle\right|^2\delta(E_f - E_i). \tag{2.2}$$

The generation rate of indirect phonons is given by

$$R_{\mathrm{ind}} = \frac{2\pi}{\hbar}\sum_{\boldsymbol{k}_i,\,\boldsymbol{k}_f}\left|\sum_j\frac{\langle\psi_f|H_{el-ph}|\psi_j\rangle\langle\psi_j|\epsilon\cdot\mathbf{p}|\psi_i\rangle}{E_j - E_i - h\nu}\right|^2 \times\delta(E_f - E_i - h\nu - \hbar\omega). \tag{2.3}$$

The electron phonon coupling $H_{el\text{-}ph}$ between the L and Γ bands has been calculated in Ref. [18].

The Seraphin-Bottka coefficients used to fit the photoreflectance spectra are extracted from first principles simulations of the real and imaginary parts of the macroscopic dielectric function ε_m. The latter is calculated within a linear-response-independent particle framework. The local density approximation (LDA) to Kohn-Sham density functional theory (DFT) is used along with plane-wave basis sets and pseudopotentials. A self-consistent ground state [26–28] for the minimum energy geometry is calculated at a plane-wave kinetic energy cutoff of 50 Ry, and a grid of $12\times12\times12$ k points used to sample the Brillouin zone. The energy gap at the Γ point is subsequently corrected with the GW approximation [21,29] (where G is the independent particle Green's function and W is the dynamically screened Coulomb interaction) using numerically converged numbers of unoccupied states and off-diagonal elements in the dielectric response function. The GW correction yields realistic optical transition energies which are used to calculate ε_m from the following expression [29]:

$$\varepsilon_m^{-1}(\omega) = 1 + \lim_{\boldsymbol{q}\to0}\frac{4\pi}{|\boldsymbol{q}^2|}\chi_{\boldsymbol{G}=0,\boldsymbol{G}'=0}(\boldsymbol{q},\omega), \tag{2.4}$$

where $\boldsymbol{q}$ is an arbitrary wave vector; $\boldsymbol{G}$ is a reciprocal lattice vector. The $\boldsymbol{q}\to\mathbf{0}$ limit is taken due to the extremely small momentum, relative to the crystal momentum, carried by a photon. The response function χ and the independent particle Green's function are calculated using the Kohn-Sham wave functions (these are obtained from a finer grid of $24\times24\times24$ k points when calculating ε_m) [29]. Local-field effects ($\chi_{(\boldsymbol{G}\neq0,\boldsymbol{G}'\neq0)}$) have a negligible effect on ε_m up to $\sim$1.5 eV above the valence band edge, and given the energy range used for the Seraphin-Bottka coefficients (see the Appendix), the extra computational load of including local-field effects in the response function is avoided and only diagonal elements of χ are obtained for the optical spectra. In addition, $\chi(\omega)$ is corrected by a material-dependent factor (a) which partially accounts for the variations in the response function (relative to an independent particle framework) due to the static long-range contribution to the exchange correlation kernel, yielding improved line shapes for optical spectra in better agreement with experiment [30,31]. The corrected response function χ_a is obtained from

$$\chi_a{}^{-1} = \chi^{-1} - a, \tag{2.5}$$

and a is related to the static dielectric constant as

$$a = \frac{1}{\chi(\omega=0)\varepsilon_m(\omega=0)}. \tag{2.6}$$

Once the real ($n = \frac{1}{\sqrt{2}}[\varepsilon_1 + \sqrt{(\varepsilon_1^2+\varepsilon_2^2)}]^{1/2}$) and imaginary parts ($k = \frac{1}{\sqrt{2}}[\sqrt{(\varepsilon_1^2+\varepsilon_2^2)} - \varepsilon_1]^{1/2}$) of the refractive index are calculated from the real (ε_1) and imaginary (ε_2) parts of ε_m, [32] the Seraphin-Bottka coefficients α and β can be obtained from the relations [33,34]:

$$\alpha = \frac{2A}{A^2+B^2}, \tag{2.7}$$

and

$$\beta = \frac{2B}{A^2+B^2}. \tag{2.8}$$

where the quantities A and B are related to n and k as

$$A = n(n^2 - 3k^2 - 1), \tag{2.9}$$

and

$$B = k(3n^2 - k^2 - 1). \tag{2.10}$$

In previous works, these relations between the Seraphin-Bottka coefficients and ε_m have been used by Sundari and Raghavan [34] to evaluate the degree of disorder present in experimental samples of tetrahedrally bonded semiconductors, and by Bondi *et al.* [33] to assess the contribution to optical spectra of suboxide composition and bonding disorder in oxide terminated Si nanowires. In this work, they provide a convenient way to extract parameters for experimental photoreflectance spectra, starting only from plane-wave pseudopotential DFT calculations.

III. MATERIAL SYNTHESIS

The unintentionally doped epitaxial Ge thin films investigated in this work were grown using a dual-chamber, solid-source molecular beam epitaxy (MBE) growth process. To this end, separate group IV and III-V reactors, connected via an ultrahigh-vacuum transfer chamber, were utilized in order to minimize interatomic diffusion and cross-species contamination during growth [35]. Starting substrates of either (001)GaAs or (001)Si, offcut 2° to 6° towards the [110] direction in order to minimize the formation of antiphase domain boundaries [36,37], were first desorbed of native oxide at 750 °C and 940 °C, respectively, noting that GaAs native oxide desorption was performed under an $\sim1\times10^{-5}$ Torr As_2 overpressure. For samples utilizing GaAs substrates, a 0.25-μm homoepitaxial GaAs buffer was grown at 650 °C (0.5 μm/h growth rate) following native oxide desorption, thereby creating an atomically flat growth surface for subsequent epitaxy. For samples utilizing Si substrates, a multistep, cyclically

annealed 2.0 μm GaAs metamorphic buffer was grown so as to bridge the lattice constants between GaAs and Si and mitigate the propagation of defects and dislocations within subsequent epitaxial III-V and Ge layers. Following GaAs buffer growth, an up to 1.9 μm linearly graded $In_xGa_{1-x}As$ metamorphic buffer was grown at 550 °C, wherein the thickness and strain grading rate were selected based on the desired strain-state of the overlying Ge epilayer, and thus Indium (In) composition of the subsequent constant-composition $In_xGa_{1-x}As$ stressor. Specifically, In stressor compositions of 11%, 15%, 17%, 24%, and 29% were selected (samples B, C, D, E, and F, respectively), corresponding to empirical strain states of 0.82%, 0.95%, 1.11%, 1.6%, and 1.94%, respectively, as determined via x-ray diffraction analysis and independently confirmed using Raman spectroscopy [38–40]. Upon completion of the $In_xGa_{1-x}As$ stressor, the samples were gradually cooled to 100 °C and immediately transferred *in vacuo* to the group IV growth chamber. Thin 15- to 240-nm Ge epilayers were then grown at 400 °C utilizing a low Ge growth rate of ~0.025 μm/h and finally cooled to room temperature following growth at a rate of 5 °C per minute, thereby minimizing relaxation and unintentional thermal stress accumulation due to the mismatch in thermal expansion coefficients between materials. Unstrained epitaxial Ge controls (sample A) were also grown on (001)GaAs and (001)Si utilizing the aforementioned procedures with the substitution of a 170-nm AlAs isolation layer grown at 600 °C (0.17 μm/h growth rate) preceeding the GaAs metamorphic buffer growth. Complete growth and materials characterization details, including sample-specific capping layer growth (samples C, D, and F) and Ge critical thickness considerations, are reported elsewhere [35,38–40].

IV. EXPERIMENTAL METHODS

Low temperature photoluminescence (PL) was utilized to obtain band-gap information of the designed materials. For sample excitation, a Ti:sapphire pulsed laser was used with a power of 0.4 W, focused on a 6-μm spot at the sample surface, giving 1.4 MW/cm^2. Samples were held inside a liquid nitrogen cryostat with temperature range from 80 to 300 K. Emission of the sample was focused through a long-pass filter to a monochromator equipped with a liquid nitrogen chilled InAs detector. For sample surface monitoring and precise focusing, a charge-coupled device (CCD) camera with an external light-emitting diode (LED) source was used during alignment, similar to a confocal microscope setup. This arm was inserted in the setup with the help of a removable 50/50 beam splitter placed prior to the focusing objective and the sample holder. This beam splitter was removed after alignment, providing full PL focused on the monochromator slit.

The photoreflectance [41] technique was used to study transition energies above the band edge. A 405-nm, 40-mW laser diode was used to perturb an electric field at the surface of the material. This results in perturbation of the complex dielectric function of the semiconductor, which in turn defines the reflectance of the semiconductor.

A broadband tungsten light source is placed in one entrance of the monochromator slit to provide a wavelength range for a reflection spectrum of the sample. A liquid nitrogen chilled detector with a long-pass filter was used to measure the reflection response.

A long-pass filter was used to cut any emission at a wavelength shorter than 1 μm and avoid second-order diffraction peaks in the spectra. A combination of long-pass filters was also used to study spectra in the 0.7–1.4-μm range and the 1.3–2.6-μm range. All samples were placed in a liquid nitrogen cryostat and chilled to 80 K.

The standard chopper modulation technique allowed tracking of the changes in reflectance with and without perturbation. This setup configuration provided detection of the photoreflectance signal with no influence of the PL on the spectral shape. Photoreflectance spectra were fitted using Franz-Keldysh (FKO) oscillation [42] and third-order derivative line shape (TDLS).

The FKO model is based on the complex Airy functions and was explained in detail by Estrera *et al.* [43], Seraphin and Bottka [44], Aspnes [45], and Batchelor *et al.* [46]. Based on their research we used the following set of equations:

$$\frac{\Delta R}{R} = \mathrm{Re}\left[C e^{i\varphi} \frac{H(z)}{(E - i\Gamma)^2} \right], \tag{4.1}$$

$$\tan\varphi = -\frac{\beta}{\alpha}, \tag{4.2}$$

$$H(z) = F(z) + iG(z), \tag{4.3}$$

$$z = \frac{1}{\hbar\theta}(E - E_c) + i\Gamma, \tag{4.4}$$

$$\Gamma = \Gamma_0 \exp\left[(E_c - E)\,\delta\right]. \tag{4.5}$$

Parameter C is a combination of amplitude parameters; $\tan\varphi$ represents the ratio of Seraphin-Bottka coefficients α and β; Γ is a broadening parameter in energy units, related to the lifetime of charge carriers, and amplitude Γ_0 is a modified nominal broadening at transition energy; δ is the Batchelor's fitting parameter, related to defects in the structure; E_c is the critical energy of the transition; $\hbar\theta$ is related to the lattice perturbation strength in the lattice:

$$\varepsilon_{\mathrm{eff}} = \frac{2\mu_{||}}{e\hbar}(\hbar\theta)^{3/2}, \tag{4.6}$$

where e is an electron charge; $\mu_{\|}$ is a joint interband effective mass of the solid; $\varepsilon_{\mathrm{eff}}$ is an effective built-in electric field in the lattice.

The functions F and G are electro-optics functions of the first and second kind [45]:

$$F(x) = \pi[\mathrm{Ai}'(x)\mathrm{Ai}'(x) - x\mathrm{Ai}(x)\mathrm{Ai}(x)] - u(-x)\sqrt{-x}, \tag{4.7}$$

$$G(x) = \pi[\mathrm{Ai}'(x)\mathrm{Bi}'(x) - x\mathrm{Ai}(x)\mathrm{Bi}(x)] - u(x)\sqrt{x}, \tag{4.8}$$

where $\mathrm{Ai}(x)$ is the Airy function and $\mathrm{Ai}'(x)$ is its derivative, $\mathrm{Bi}(x)$ is the Airy function of second kind and $\mathrm{Bi}'(x)$ is its derivative and $u(x)$ represents the unit step function, taking a value of 1 for positive x and 0 elsewhere. It should be noted that the critical point $E = E_c$ is omitted from the fit due to resultant infinities in F and G.

The TDLS approximation was first used for PR approximation by Aspnes [47]. He stated that in the case of low-perturbation field, the relative change in reflection can be

TABLE I. Description of Ge sample structures.

Sample	Strain (%)	Cap	Structure	Ge thickness (nm)
A	0	No	Ge	Bulk
B	0.82	No	$Ge/In_{0.11}Ga_{0.89}As/GaAs/Si$	40
C	0.95	Yes	$GaAs/Ge/In_{0.16}Ga_{0.84}As/GaAs$	15
D	1.11	No	$Ge/In_{0.17}Ga_{0.83}As/GaAs/Si$	30
E	1.6	No	$Ge/In_{0.24}Ga_{0.76}As/GaAs$	28
F	1.94	Yes	$InGaAs/Ge/In_{0.29}Ga_{0.71}As/GaAs$	15

defined by

$$\frac{\Delta R}{R} = \mathrm{Re}\left[\frac{C}{E^2} e^{i\varphi} (E - E_c + i\Gamma)^{-n}\right], \tag{4.9}$$

where C, Γ, and φ have meanings similar to the definitions above; $n = 3$ for the two-dimensional parabolic model densities of states. In his work Aspnes omits the terms corresponding to $1/E^2$; however, in the case of large broadening it can play a significant role and hence we included it in the model.

A simplified TDLS model is often used [48–50], but it is valid only in the case of low and uniform electrical perturbation of the crystal material [51,52]. Low perturbation can be estimated from the experiment as the case of $\Delta R/R \leqslant 10^{-4}$ [47].

Any source of background noise, such as PL, can generate an offset on the PR spectra $dR + R_0$. This offset is normally compensated by the lock-in, but can have some effect on the graph. For this purpose, an offset parameter R_0 was added to the fitting.

V. RESULTS AND DISCUSSIONS

In this work, Ge samples with applied biaxial tensile strain from 0% to 1.94% are studied. Ge strain, structure, and thickness parameters are summarized in Table I. Some samples (C, F) have a GaAs or InGaAs capping layer grown over the strained Ge and are used only in the PL analysis.

A. Photoluminescence

Figure 1(a) depicts PL of sample A (Table I), which is a Ge/AlAs/GaAs/Si layer structure. Ge has a 0.05% smaller lattice parameter than AlAs, so in this sample a thick 240-nm Ge layer on a 170 nm layer of AlAs which is well above critical thickness and results in no strain ($\varepsilon = 0\%$).

The peaks of the emission for this and the following PL spectra are fitted using a Lorentzian function. The sample A peaks are centered at 0.725 eV (1710 nm) and 0.706 eV (1756 nm) at 80 K. $\mathbf{k} \cdot \mathbf{p}$ modeling of energy bands showed the the L valley to light holes (L-lh) transition with energy 0.746 eV. Measured peaks correspond to longitudinal acoustic (LA) and transverse optical (TO) phonon-assisted recombination, similar to that reported in [53]. At low temperature there are fewer free phonons in the crystal; phonon-assisted recombination from the L band generates a phonon. For this reason at low temperature emission energy is lower than the energy gap with the rest of the recombination energy transferred into a phonon. At high temperature there are more phonons in the crystal and recombination happens after absorption of a free phonon. This results in increase of emission energy; in addition a phonon is not generated, but absorbed. Redshift of the PL emission, as the temperature changes from 80 to 240 K, can be seen in Fig. 1(b), corresponding to temperature dependence of the L valley. Temperature dependence of the L band is also compared with absorption experiments [22].

Sample C (Table I) is a structure of layers $GaAs/Ge/In_{0.16}Gas_{0.84}As/GaAs$ with GaAs and Ge layer thickness of 15 nm each. It has an $\varepsilon = 0.95\%$ biaxial tensile strain in the Ge layer. This sample provided bright PL, shown in Fig. 2(a). Peak emission at 80 K corresponds to 0.687 eV (1805 nm) band-gap energy. As can be seen there is a 40-meV (98 nm) redshift in comparison to the sample with no strain, which is expected due to the shrinking of the energy gap under tensile strain for such a thin sample. Bright emission can be explained via the compounding effects of strain-dependent gain enhancement, prohibitively large energy separations between the L and Γ conduction band minima, and momentum contribution to the indirect L-valley light holes (lh) recombination path from exciton-generated longitudinal acoustic (LA) phonons [39]. In the former case, several theoretical [54–56] and experimental

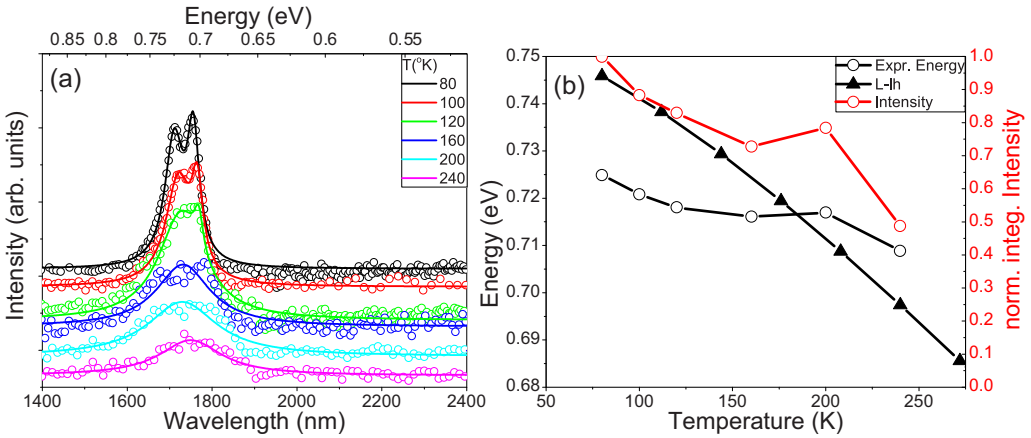


FIG. 1. (a) Photoluminescence spectra of Ge/AlAs (sample A) under $\varepsilon = 0\%$ biaxial tensile strain depending on temperature; (b) experimental (circles) and calculated (triangles) peak energy (black line) and normalized integrated intensity (red line) versus temperature.

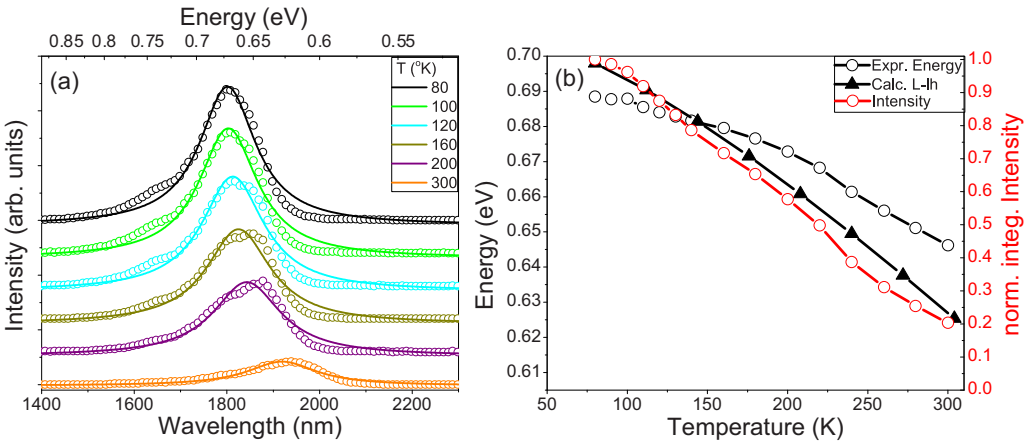


FIG. 2. (a) Photoluminescence spectra of GaAs/Ge/$In_{0.16}Ga_{0.84}As$/GaAs (sample C) under $\varepsilon = 0.95\%$ biaxial tensile strain depending on temperature; (b) experimental (circles) and calculated (triangles) peak energy (black line) and normalized integrated intensity (red line) versus temperature.

[57,58] studies have demonstrated the effects of increasing tensile strain and doping concentrations on optical gain (or absorption) in Ge films. From these previous results, one would expect that the lower-energy spectral features would exhibit higher relative PL intensities when compared with the higher-energy features, as will be seen later in Fig. 5 comparing samples with 0% and 0.95% of strain.

Next, sample E (Table I) has a similar composition with some increase in strain. This is a Ge/$In_{0.24}Ga_{0.76}As$/GaAs structure with Ge layer thickness of 28 nm. Biaxial tensile strain applied to Ge in this case is equal to $\varepsilon = 1.6\%$. The center of emission at 80 K corresponds to 0.631 eV (1944 nm). An interesting behavior in the PL spectra is observed with increasing temperature as seen in Fig. 3(b). The PL spectra redshifts to 0.614 eV (2020 nm) at 160 K before blueshifting to 0.640 eV (1938 nm) as the temperature further increases to 290 K. Also, the broad nature of the PL emission for this sample is noticeable in Fig. 3(a). This sample corresponds to the indirect-to-direct band-gap transition point for the Ge according to 30-band $\mathbf{k}\cdot\mathbf{p}$ simulation shown in Fig. 8(b). Reasons for this blueshift include different charge carrier lifetimes inside the indirect L valley and direct Γ valley as well as the presence of nonradiative recombination inside the structure. Defects within the structure strongly suppress emission from the indirect L-valley transition, due to the slow recombination rate in the indirect channel. Indirect transitions require a phonon for motion in k space. For this reason, the probability of two carriers (an electron and a hole) coinciding is higher than that for three entities (an electron, a hole, and a phonon), so transitions from the direct Γ valley have a faster recombination rate. This also means that leakage of charge carriers through nonradiative recombination channels has less effect on direct band-gap emission compared to indirect band-gap emission. This results in domination of the direct band-gap emission at higher temperatures over the indirect and emission switch, which gives a blueshift with increase of temperature.

Another point is that according to Fermi-Dirac distribution, at higher temperatures there is a broad distribution of energies of the charge carriers and thus a higher possibility of recombination with energies above the energy gap. If the Γ valley is slightly above the L valley, emission from the Γ valley becomes more pronounced at higher temperature, which is observed in

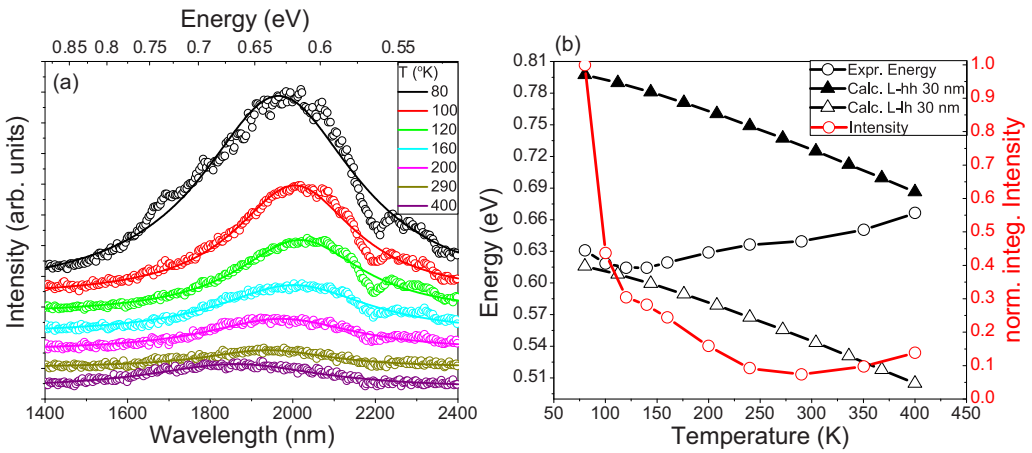


FIG. 3. (a) Photoluminescence spectra of Ge/$In_{0.24}Ga_{0.76}As$ (sample E) under $\varepsilon = 1.6\%$ biaxial tensile strain depending on temperature; (b) experimental (circles) and calculated (triangles) peak energy (black line) and normalized integrated intensity (red line) versus temperature.

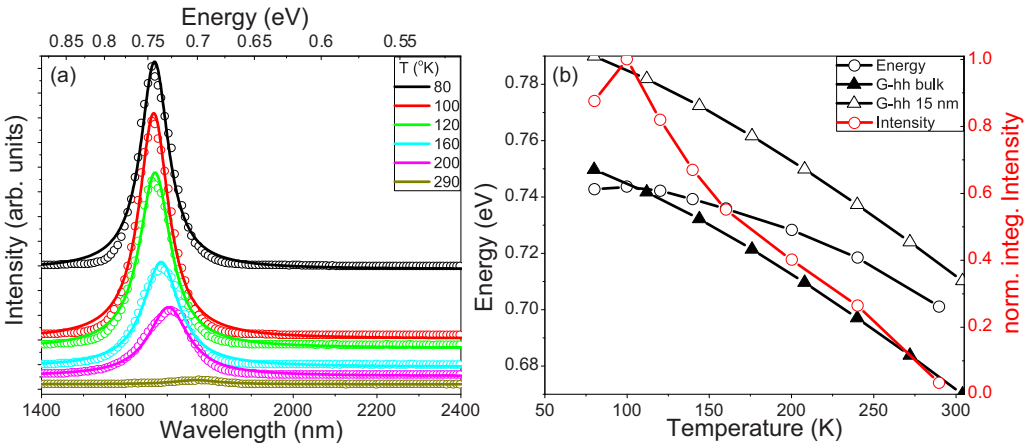


FIG. 4. (a) Photoluminescence spectra of InGaAs/Ge/$In_{0.29}Ga_{0.71}As$/GaAs (sample F) under $\varepsilon = 1.94\%$ biaxial tensile strain depending on temperature; (b) experimental (circles) and calculated (triangles) peak energy (black line) and normalized integrated intensity (red line) versus temperature.

sample E. High density of states in the heavy holes (hh) valley in comparison with the lh valley in the case of large population also results in further increase of the emission blueshift. Similar results on the transition between indirect and direct band-gap emission with increase of temperature in Ge have previously been reported at temperatures >300 K [59–64]. The low temperature (160 K) observed in our experiment is explained as a close indirect-to-direct crossover point for sample E (see Fig. 4).

Sample F (Table I) has a structure of Ge/$In_{0.29}Ga_{0.71}$ As/GaAs with the highest concentration of In in the buffer layer presented in this work. This concentration of In provides a biaxial tensile strain of $\varepsilon = 1.94\%$. The center of the PL peak at 80 K for sample F is at 0.739 eV (1678 nm). This emission corresponds to the Γ-hh transition which according to the 30-band $\mathbf{k} \cdot \mathbf{p}$ simulation (Fig. 8) has energy 0.762 eV. It has been reported that experimental collection geometries normal to the sample surface (i.e., in the z direction) favor conduction band coupling with the hh valence band [65]. This gives an additional credence to a pronounced blueshift of emission in sample E. The high intensity of the sample F emission is consistent with emission from the direct band gap. It blueshifts by 40 meV (96 nm) at room temperature, providing temperature dependence of the Γ valley.

Spectra of the samples with varying tensile strain measured at $T = 80$ K are summarized in Fig. 5 with intensity normalized to sample F. It is clear that with increase of strain up to 1.6% there is a redshift in sample emission, but for the sample F with the highest strain (1.94%) its emission energy is higher than that of the unstrained sample A, which also proves a transition not to lh, but to hh. Relaxation of the strain in sample F, which could be proposed to explain the blueshift of the emission, is not consistent with sample F having the highest PL intensity of the discussed samples (see Fig. 5). Furthermore, the sample with the highest strain has the highest emission intensity, which is a feature of direct transition. Growth of a cap layer is known to result in marked improvements of the optical properties of semiconductor hetero- and nanostructures and this effect is usually associated with reduction in the large concentration of nonradiative defects (e.g., dangling bonds) usually present at the sample surface [66]. In our studies, the difference in PL intensity for the capped and uncapped samples was about 30% in favor of uncapped structures (Fig. 10 in the Appendix) so adding a capping layer is not reducing or increasing nonradiative recombination channels and not influencing carrier density in the Ge layer. (It is possible that the second interface between Ge and III-V material could generate additional defects in the quantum well).

B. Photoreflectance

For a closer examination of the tensile strain effect on the direct band gap of Ge, the samples were studied with photoreflectance spectroscopy. Experimental PR spectra were fitted using two models: TDLS and complex Airy discussed previously. A high number of critical energies could improve fit quality; however, they could also generate artificial peaks which compensate deviation of the model and experiment. To keep consistency between samples with different strain we used a minimum number of critical energies in all fits: two

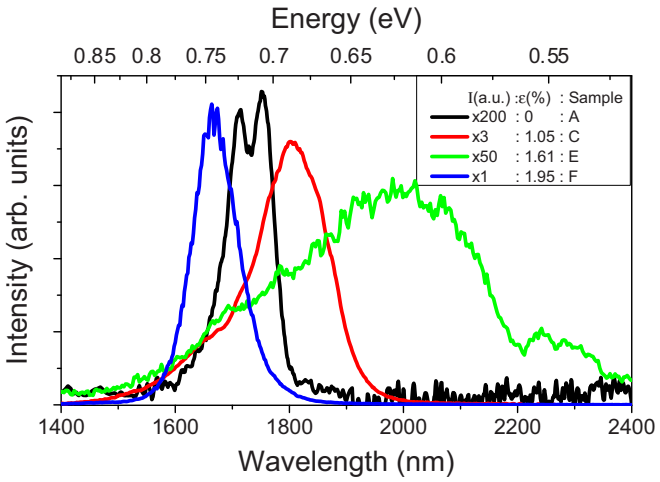


FIG. 5. PL spectra at different biaxial tensile strain (samples A, C, E, F) at 80 K.

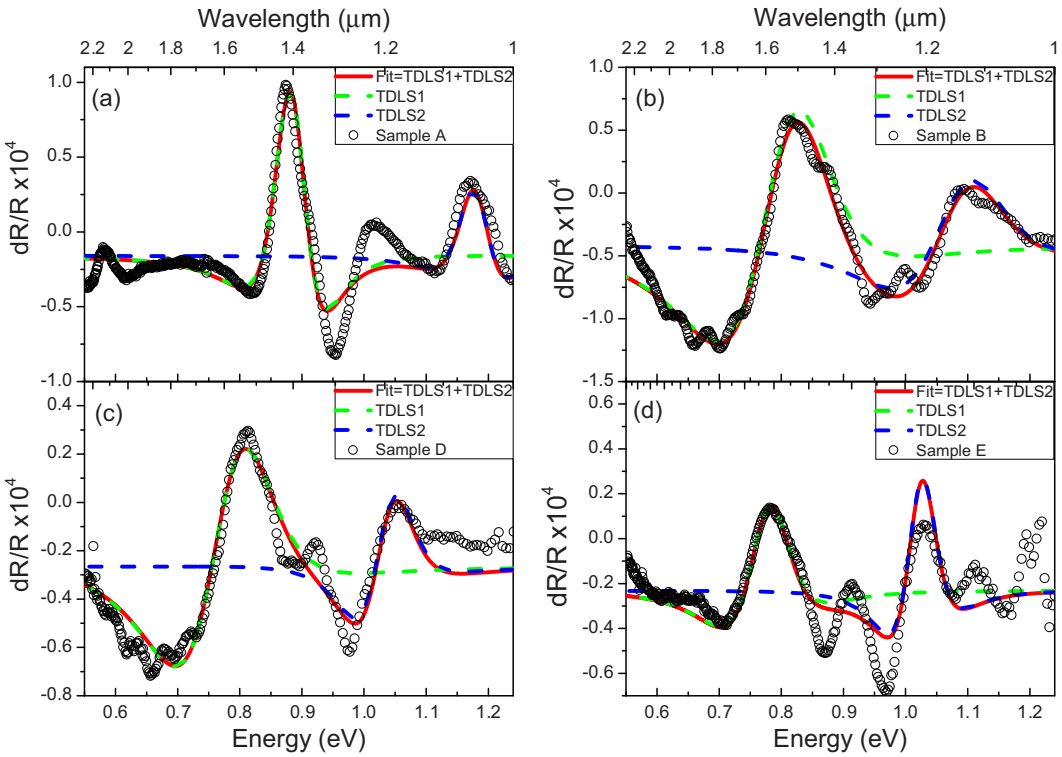


FIG. 6. Photoreflectance spectrum of Ge under ε: (a) sample A, 0%; (b) sample B, 0.82%; (c) sample D, 1.11%; (d) sample E, 1.6% biaxial tensile strain at 80 K, fitted with two TDLS functions. Open circles correspond to the experimental data, red lines are the fit including two TDLSs, depicted in green and blue, respectively.

critical energies to fit only major spectral features. In the end of this section there is a simulation of PR spectra which includes all quantum levels of the 0.55–1.24-eV spectral range.

TDLS fits of PR spectra of the samples A, B, D, E are shown in Figs. 6(a)–6(d) respectively. Since Seraphin-Bottka coefficients of a semiconductor are slowly changing with the wavelength [67,68] we used the same φ parameter for all critical energies within a fit. Figure 6 has experimental points with the fitted curve overlaid including separate lines for each TDLS feature to indicate the contribution of each. The PR spectrum of the unstrained Ge sample A [Fig. 6(a)] at 80 K provided a critical point at 0.889 eV, which is close to the theoretically expected value of the Γ-hh transition equal to 0.881 meV. The critical point for the second TDLS feature was found at 1.183 eV, which is close to the predicted split-off band at 1.177 eV.

All PR critical energies are close to Γ-hh and split-off band transition energies obtained from the $\mathbf{k}\cdot\mathbf{p}$ calculation (Fig. 8). The reason why Γ-hh transitions are seen rather than Γ-lh transitions originates from higher electron-hole coupling for heavy holes over light holes [65], also mentioned in the PL discussion of sample E. For most of the spectra, some spectral features are visible at the expected values of the Γ-lh transition; however, these are too faint to make a clear assignment of a signal from this transition or obtain a reliable fit.

These weak oscillations are particularly noticeable in Fig. 6(b) for sample B with 0.82% strain. Notwithstanding the possibility of subband transitions, these most likely originate from Fabry-Perot oscillations of the light in the optical cavity created between the top and bottom edges of the sample structure. Thin layers create interference of the light which can affect the spectral shape [69] and in some cases can generate a destructive interference of the PR signal. The absence of a signal corresponding to emission from the L band in the PR spectra of the thick unstrained Ge (sample A) adds further credence to this hypothesis. With increasing strain, the critical energy obtained from the fitting exhibits a redshift as expected from the $\mathbf{k}\cdot\mathbf{p}$ simulation.

Sample D with Ge under 1.11% strain [Fig. 6(c)] was grown without a cap layer on top of the Ge. Critical energies corresponding to Γ-hh and the split-off band in this case are found to be 0.780 and 1.033 eV. Capped samples C and F (Table I), as well as others not presented in this work, did not give any detectable PR response from Ge. This originates from the fact that perturbation of the semiconductor by the reflected laser light decreases exponentially with the depth of the material. Besides that, the Ge PR response is created from perturbation of the surface states of Ge which are not present in the capped samples.

PR spectra of sample E (Table I) with $\varepsilon = 1.6\%$ tensile strain are presented in Fig. 6(d). The critical points for this sample are at 0.778 and 1.023 eV. The spectral feature in between these critical points could correspond to an additional critical point; however, a similar feature is observed in the unstrained sample A between Γ-hh and the split-off band [Fig. 6(a)] with no subband transition that can be attributed to this energy. Therefore deviation between the theoretical model and the experimentally fitted data can also be attributed not to another subband energy, but to imperfection of the TDLS model.

TABLE II. TDLS fit parameters.

Sample	Strain, ε 8(%)	Function	Amplitude, C	Phase, φ (rad)	Broadening, Γ (eV)	Energy, E (eV)
A	0	TDLS 1	-4.781×10^{-8}	3.798	0.05907	0.889
		TDLS 2	2.882×10^{-7}	3.798	0.1617	1.174
		Offset	-2.236×10^{-5}			
B	0.82	TDLS 1	2.546×10^{-7}	3.970	0.147	0.806
		TDLS 2	2.212×10^{-7}	3.970	0.148	1.084
		Offset	-4.25×10^{-5}			
D	1.11	TDLS 1	8.223×10^{-8}	3.704	0.131	0.780
		TDLS 2	1.789×10^{-8}	3.704	0.078	1.033
		Offset	-2.680×10^{-5}			
E	1.6	TDLS 1	1.454×10^{-8}	4.379	0.085	0.778
		TDLS 2	1.162×10^{-8}	4.379	0.060	1.023
		Offset	-2.324×10^{-5}			

All fitting parameters for TDLS fits are summarized in Table II. With an increase of strain, there is an expected redshift for the first critical point in energy from 0.89 eV for the unstrained sample (sample A) to 0.78 eV for the 1.6% tensile strained sample (sample E).

Since the TDLS model shows some deviation with the experiment, an Airy fit for the samples A, B, D, and E is also performed [Figs. 7(a)–7(d)]. Similar to TDLS each fit was performed for two critical points. Since perturbation is the same for all energy levels, the $\hbar\theta$ parameter for both critical points is also equal. All Airy fit parameters can be found in Table III of the Appendix. One can see that for samples B and E the fitting parameter $\hbar\theta < \Gamma/3$ which means they are in the low-field regime, while for samples A and D, $\hbar\theta \sim \Gamma$ which corresponds to the intermediate-field measurements. Effective built-in electric field was also estimated from the $\hbar\theta$ parameter and mobility μ. It should be noted that sample B has a lower value of effective built-in electric field (310 kV/cm) than that of sample A (153 kV/cm). For this reason, a clear selection of either TDLS or Airy functions for photoreflectance spectra based on the value of $\hbar\theta$ is not possible in our case. Comparing the quality of TDLS and Airy fit one can note a better coverage of Airy fits for samples A and E. There is almost no difference for samples B and D. Critical points of Airy and TDLS fits

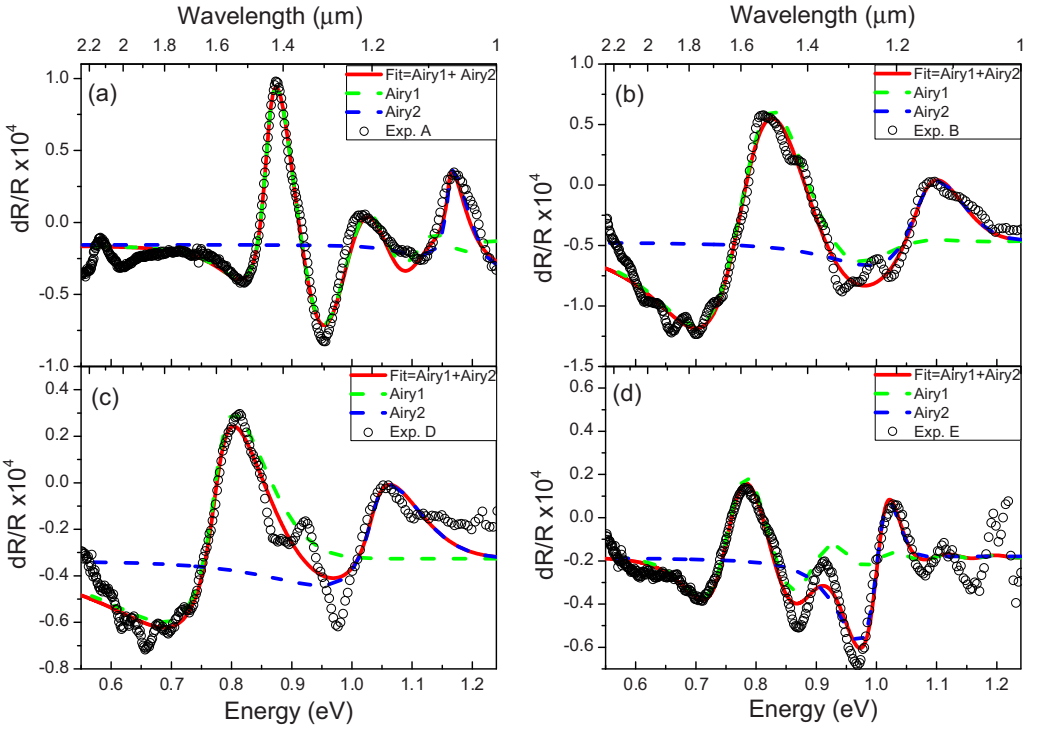


FIG. 7. Photoreflectance spectrum of Ge under ε: (a) 0%, (b) 0.82%, (c) 1.11%, (d) 1.6% biaxial tensile strain at 80 K, fitted with two Airy functions. Dotted lines correspond to the experimental data, red lines are the fit including two Airy functions, depicted in green and blue, respectively.

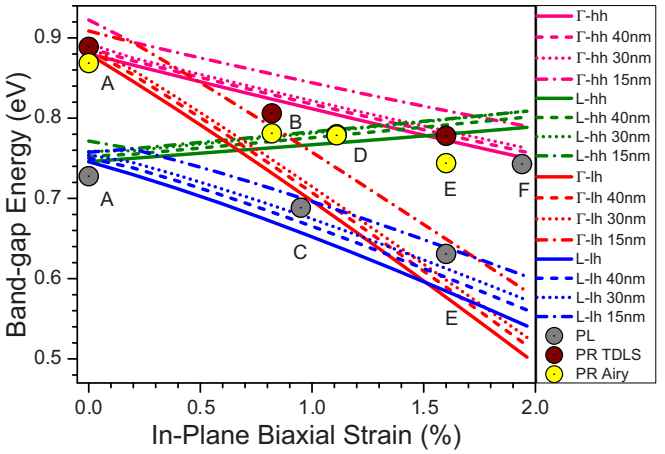


FIG. 8. Theoretical band-gap-strain dependence for Ge calculated using a 30×30 $\mathbf{k} \cdot \mathbf{p}$ model taking into account quantization-induced band-gap enhancement at decreased ε-Ge layer thicknesses for 40-, 30-, and 15-nm quantum wells. Experimental peaks given by PL and PR data are shown as circles over theoretically predicted transitions from Γ and L valley to light (lh) and heavy (hh) holes.

in addition to PL peak points are shown on the top of the theoretically calculated band energies in Fig. 8.

TDLS critical points of samples A, B, D, E follow the trend of the theoretically calculated Γ-hh in Fig. 8. In addition to this, the PL peak of sample F follows the trend of the PR critical points. Taking into account the increase of PL intensity (see Fig. 5) this gives an additional confirmation of the direct band-gap nature of PL emission from the sample with the highest strain.

The photoreflectance spectrum contains information on all critical points of the band structure. Due to quantum confinement in the thin Ge layer, electron and hole energy levels are situated not at the band edge, but at a number of subband energy levels. This affects the quality of fitting in Figs. 6 and 7. To make a PR model that includes all quantum energy levels, the TDLS parameters for all subbands are calculated directly.

The optical coupling, given by the square of the momentum matrix element between the electron-hole wave functions, is used as a relative amplitude parameter for each critical point. Density of states (DOS) is related to charge carrier lifetime and thus is taken as a broadening with a general scaling coefficient for all subband energies. Subband energies, DOS, and broadening (Fig. 11 in the Appendix) are calculated for 40-nm quantum confinement for $\varepsilon = 0.82\%$ biaxial tensile strain and for 30-nm quantum confinement for $\varepsilon = 1.11\%$. Phase parameters are calculated from Seraphin-Bottka coefficients (Fig. 12 in the Appendix), assuming equality of $e^{i\varphi}$ terms in Airy and TDLS functions. The resulting TDLS functions are obtained from the model and are depicted in Fig. 9. As seen from those graphs the PR models of 0%, 0.82%, and 1.11%

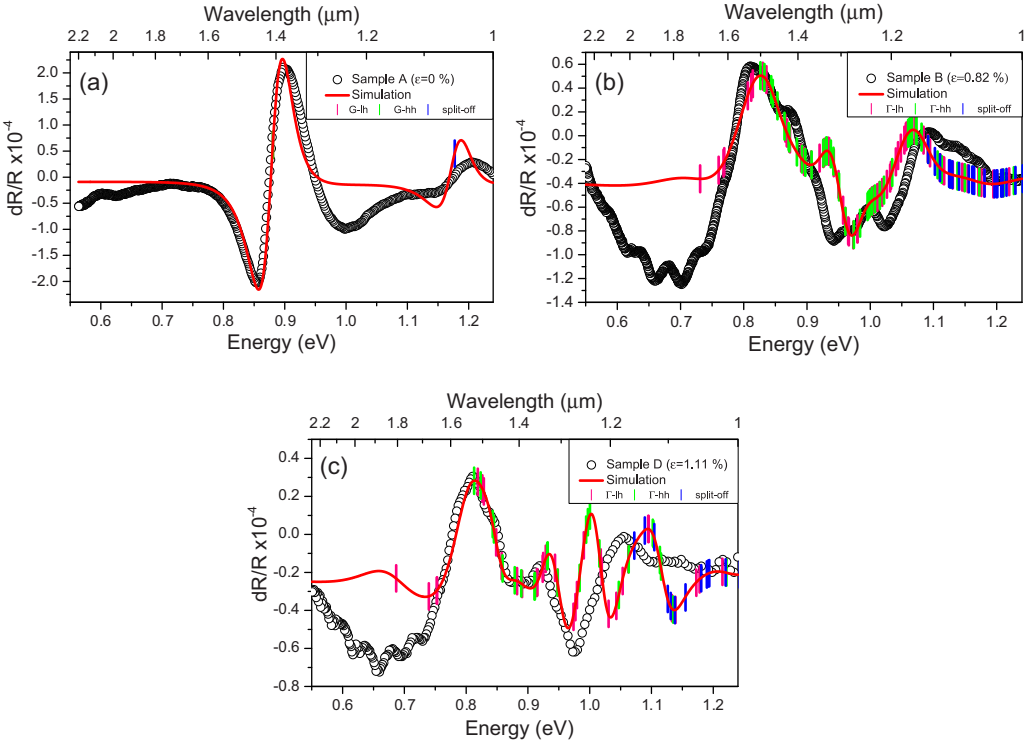


FIG. 9. Full photoreflectance spectra simulation on the top of experimental data for (a) unstrained sample; (b) $\varepsilon = 0.82\%$ model over sample D spectra; (c) $\varepsilon = 1.11\%$ model over sample E spectra. Γ-lh, Γ-hh, and split-off subband transition energies are depicted as vertical dashes.

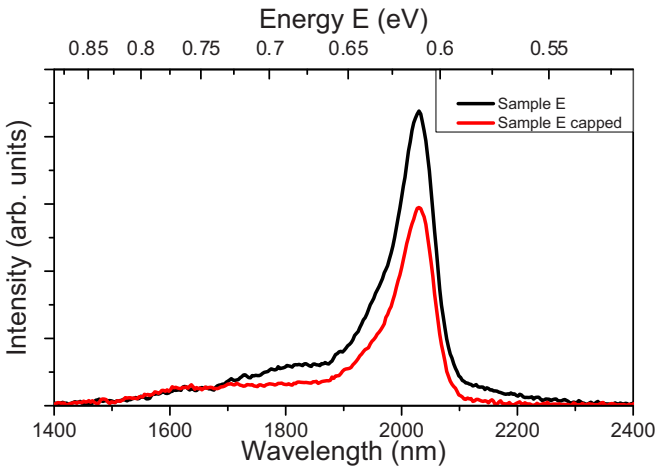


FIG. 10. Photoluminescence spectra of $Ge/In_{0.24}Ga_{0.76}As/GaAs$ (sample E) and $InGaAs/Ge/In_{0.24}Ga_{0.76}As/GaAs$ (sample E capped) under $\varepsilon = 1.6\%$ biaxial tensile strain at 8 K.

biaxial tensile strain correspond to experimental samples A, B, and D (Table I). There are a number of assumptions made during this simulation, such as ideal surface of Ge quantum well, and homogeneous strain within the Ge layer, as well as general TDLS simplifications. We also simulated Seraphin-Bottka coefficients without including quantum constrains. These simplifications have an effect on the simulation quality; however, this simulation gives a number of features visible in the experimental spectra and has quality comparable with the other [70]. We should also mention a certain deficit of PR spectra simulations even though PR spectra require careful interpretation.

VI. CONCLUSIONS

In this article, we discussed the band structure of germanium under tensile strain. Utilizing $\mathbf{k} \cdot \mathbf{p}$ modeling, band transitions were calculated numerically and then confirmed in the experimental study. Using photoluminescence, the indirect L valley was determined at various strain and temperatures. The photoreflectance identified the change of direct band gap with increase of strain and confirmed theoretical assumptions about high heavy hole coupling in germanium. Photoreflectance spectra were analyzed using TDLS and FKO models and compared with simulated photoreflectance spectra. The TDLS approximation fit had the advantage in obtaining energy values close to the Γ-hh and split-off transition energies obtained from $\mathbf{k} \cdot \mathbf{p}$ simulation, while the Airy fit showed better coverage of the experimental data. The indirect-to-direct crossover was reached in this study between the samples with 1.6% and 1.94% lattice mismatch of Ge and InGaAs layers.

ACKNOWLEDGMENTS

Thanks to David Williams for the discussions during preparation of this paper. G.G.-D. and M.G. acknowledge the use of computational facilities at the Atomistic Simulation Centre in Queen's University Belfast and the support from the Department for the Employment of Northern Ireland. The research in this publication was supported under the US-Ireland R&D Partnership Program by Science Foundation Ireland (SFI) Grant No. SFI/14/US/I3057, by InvestNI Grant No. USI-073, by the National Science Foundation (US) Grants No. ECCS-1348653 and No. ECCS-1507950.

APPENDIX

In Fig. 10 PL spectra are plotted for the capped and uncapped samples with the same amount of strain. Figure 11 depicts subband energies and DOS calculated for 40-nm

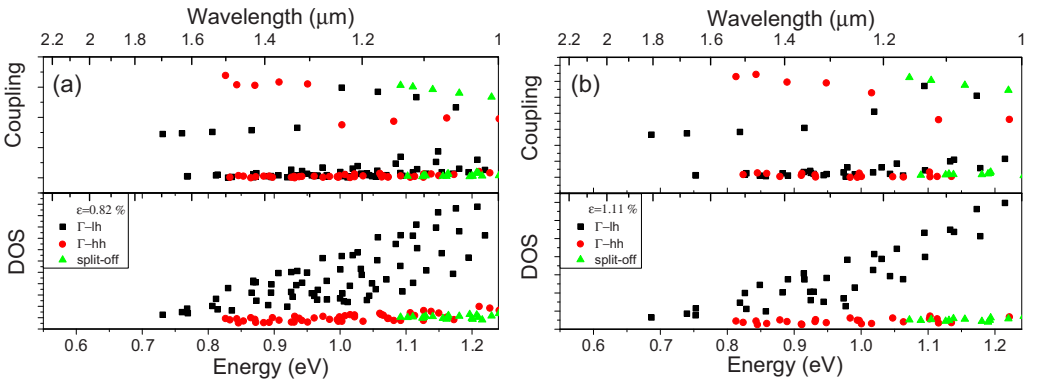


FIG. 11. $\mathbf{k} \cdot \mathbf{p}$ calculations of electron-hole wave-function coupling and density of states (DOS) for subband transition energies in (a) 40-nm Ge quantum well with $\varepsilon = 0.82\%$ biaxial tensile strain; (b) 30-nm Ge quantum well with $\varepsilon = 1.11\%$ biaxial tensile strain.

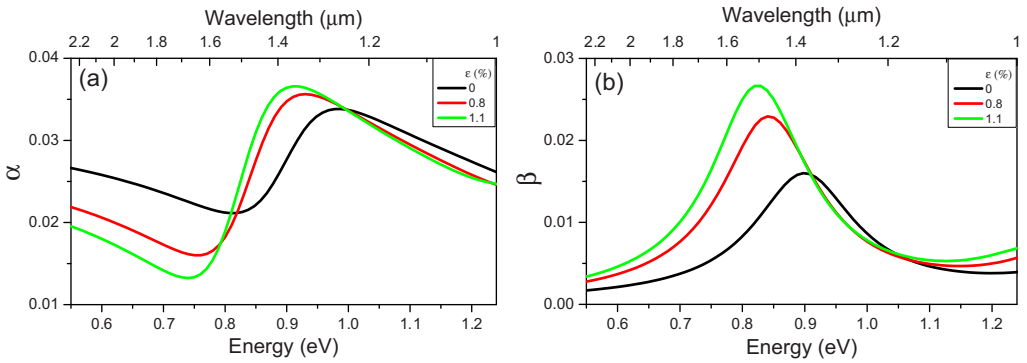


FIG. 12. Calculated (a) α and (b) β Seraphin-Bottka coefficients in Ge at 80 K and at 0%, 0.8%, and 1.1% biaxial tensile strain.

quantum confinement for $\varepsilon = 0.82\%$ biaxial tensile strain and for 30-nm quantum confinement for $\varepsilon = 1.11\%$. The Seraphin-Bottka coefficients α and β which enter the experimental photoreflectance spectra are calculated using the methodology described in Sec. II. The real (n) and imaginary parts (k) of the refractive index are calculated from ε_m using Eq. (2.4), which in turn yields α and β from Eqs. (2.7) to (2.10). In Fig. 12, α and β are plotted as a function of energy and wavelength for unstrained Ge and for two values (0.8% and 1.1%) of biaxial tensile strained Ge. For details of Airy fit parameters see Table III.

TABLE III. Airy fit parameters.

Sample	Strain, ε (%)	Function	Amplitude C (a.u.)	Phase, φ (rad)	Pertur-bation, $\hbar\theta$ (eV)	Efficient built-in electric field, ε_{eff} (kV/cm)	Batchelor, δ (eV^{-1})	Broadening, Γ (eV)	Energy, E (eV)
A	0	Airy 1	0.001003	2.965	0.06928	153.40	11.23	0.05013	0.8687
		Airy 2	0.0005207	2.965	0.06928		0	0.2844	1.170
		offset	-2.559×10^{-5}						
B	0.82	Airy 1	0.002095	1.706	0.1095	309.66	2.137	0.5292	0.7811
		Airy 2	0.0009086	1.706	0.1095		7.266	0.3495	1.081
		Offset	-4.611×10^{-5}						
D	1.11	Airy 1	0.0003073	2.034	0.1555	526.89	11.09	0.1283	0.7786
		Airy 2	−0.0002524	2.034	0.1555		11.79	0.1224	1.039
		offset	-3.264×10^{-5}						
E	1.6	Airy 1	0.0006077	1.972	0.06432	141.44	0	0.5670	0.7440
		Airy 2	−0.001164	1.972	0.06432		25.53	0.4594	1.015
		Offset	-1.803×10^{-5}						

[1] D. A. B. Miller, Int. J. Optoelectron. **11**, 155 (1997).

[2] K. Ohashi, K. Nishi, T. Shimizu, M. Nakada, J. Fujikata, J. Ushida, S. Toru, K. Nose, M. Mizuno, H. Yukawa, M. Kinoshita, N. Suzuki, A. Gomyo, T. Ishi, D. Okamoto, K. Furue, T. Ueno, T. Tsuchizawa, T. Watanabe, K. Yamada *et al.*, Proc. IEEE **97**, 1186 (2009).

[3] D. A. B. Miller, Proc. IEEE **97**, 1166 (2009).

[4] C. Gunn, IEEE Micro **26**, 58 (2006).

[5] L. Liu, R. Kumar, K. Huybrechts, T. Spuesens, G. Roelkens, E.-J. Geluk, T. de Vries, P. Regreny, D. Van Thourhout, R. Baets, and G. Morthier, Nat. Photonics **4**, 182 (2010).

[6] A. W. Fang, H. Park, O. Cohen, R. Jones, M. J. Paniccia, and J. E. Bowers, Opt. Express **14**, 9203 (2006).

[7] J. Van Campenhout, R. P. Rojo, P. Regreny, C. Seassal, D. Van Thourhout, S. Verstuyft, L. Di Cioccio, J.-M. Fedeli, C. Lagahe, and R. Baets, Opt. Express **15**, 6744 (2007).

[8] M. Lebby, S. Ristic, N. Calabretta, and R. Stabile, in *Optical Interconnects for Data Centers*, edited by T. Tekin, R. Pitwon, A. Håkansson, and N. Pleros (Elsevier, Amsterdam, 2017), pp. 97–120.

[9] J.-M. Fedeli, B. Bakir, and N. Olivier, Proc. SPIE **7942**, 79420O (2011).

[10] Z. Wang, B. Tian, M. Pantouvaki, W. Guo, P. Absil, J. Van Campenhout, C. Merckling, and D. Van Thourhout, Nat. Photonics **9**, 837 (2015).

[11] S. Wirths, R. Geiger, N. von den Driesch, G. Mussler, T. Stoica, S. Mantl, Z. Ikonic, M. Luysberg, S. Chiussi, J. M. Hartmann, H. Sigg, J. Faist, D. Buca, and D. Grützmacher, Nat. Photonics **9**, 88 (2015).

[12] S. Gupta, B. Magyari-Köpe, Y. Nishi, and K. C. Saraswat, J. Appl. Phys. **113**, 073707 (2013).

[13] S. Biswas, J. Doherty, D. Saladukha, Q. Ramasse, D. Majumdar, M. Upmanyu, A. Singha, T. Ochalski, M. A. Morris, and J. D. Holmes, Nat. Commun. **7**, 11405 (2016).

[14] R. A. Soref and L. Friedman, Superlattices Microstruct. **14**, 189 (1993).

[15] P. H. Lim, S. Park, Y. Ishikawa, and K. Wada, Opt. Express **17**, 16358 (2009).

[16] K. Wang, Q. Gong, H. Zhou, C. Kang, J. Yan, Q. Liu, and S. Wang, Appl. Surf. Sci. **291**, 45 (2014).

[17] M. V. Fischetti and S. E. Laux, J. Appl. Phys. **80**, 2234 (1996).

[18] F. Murphy-Armando and S. Fahy, J. Appl. Phys. **109**, 113703 (2011).

[19] D. Mohata, S. Mookerjea, A. Agrawal, Y. Li, T. Mayer, V. Narayanan, A. Liu, D. Loubychev, J. Fastenau, and S. Datta, Appl. Phys. Express **4**, 024105 (2011).

[20] D. Rideau, M. Feraille, L. Ciampolini, M. Minondo, C. Tavernier, H. Jaouen, and A. Ghetti, Phys. Rev. B **74**, 195208 (2006).

[21] M. S. Hybertsen and S. G. Louie, Phys. Rev. B **34**, 5390 (1986).

[22] Y. P. Varshni, Physica (Amsterdam) **34**, 149 (1967).

[23] N. Pavarelli, T. J. Ochalski, F. Murphy-Armando, Y. Huo, M. Schmidt, G. Huyet, and J. S. Harris, Phys. Rev. Lett. **110**, 177404 (2013).

[24] W. A. Harrison, J. Appl. Phys. **110**, 113715 (2011).

[25] S. Paul, J. B. Roy, and P. K. Basu, J. Appl. Phys. **69**, 827 (1991).

[26] W. Kohn and L. J. Sham, Phys. Rev. **140**, A1133 (1965).

[27] J. P. Perdew and Y. Wang, Phys. Rev. B **45**, 13244 (1992).

[28] P. Giannozzi, S. Baroni, N. Bonini, M. Calandra, R. Car, C. Cavazzoni, D. Ceresoli, G. L. Chiarotti, M. Cococcioni, I. Dabo, A. Dal Corso, S. de Gironcoli, S. Fabris, G. Fratesi, R. Gebauer, U. Gerstmann, C. Gougoussis, A. Kokalj, M. Lazzeri, L. Martin-Samos *et al.*, J. Phys.: Condens. Matter **21**, 395502 (2009).

[29] A. Marini, C. Hogan, M. Grüning, and D. Varsano, Comput. Phys. Commun. **180**, 1392 (2009).

[30] S. Botti, F. Sottile, N. Vast, V. Olevano, L. Reining, H. C. Weissker, A. Rubio, G. Onida, R. Del Sole, and R. W. Godby, Phys. Rev. B **69**, 155112 (2004).

[31] J. A. Berger, Phys. Rev. Lett. **115**, 137402 (2015).

[32] M. Fox, *Optical Properties of Solids* (Oxford University Press, Oxford, 2001).

[33] R. J. Bondi, S. Lee, and G. S. Hwang, ACS Nano **5**, 1713 (2011).

[34] S. T. Sundari and G. Raghavan, Appl. Phys. Lett. **86**, 241906 (2005).

[35] P. D. Nguyen, M. B. Clavel, P. S. Goley, J.-S. Liu, N. P. Allen, L. J. Guido, and M. K. Hudait, IEEE J. Electron Dev. Soc. **3**, 341 (2015).

[36] S. M. Ting and E. A. Fitzgerald, J. Appl. Phys. **87**, 2618 (2000).

[37] M. K. Hudait and S. B. Krupanidhi, J. Appl. Phys. **89**, 5972 (2001).

[38] M. B. Clavel and M. K. Hudait, IEEE Electron Dev. Lett. **38**, 1196 (2017).

[39] M. Clavel, D. Saladukha, P. S. Goley, T. J. Ochalski, F. Murphy-Armando, R. J. Bodnar, and M. K. Hudait, ACS Appl. Mater. Interfaces **7**, 26470 (2015).

[40] M. Clavel, P. Goley, N. Jain, Y. Zhu, and M. K. Hudait, IEEE J. Electron Dev. Soc. **3**, 184 (2015).

[41] R. N. Bhattacharya, H. Shen, P. Parayanthal, F. H. Pollak, T. Coutts, and H. Aharoni, Phys. Rev. B **37**, 4044 (1988).

[42] L. V. Keldysh, Sov. Phys. JETP **6**, 763 (1958).

[43] J. P. Estrera, W. M. Duncan, and R. Glosser, Phys. Rev. B **49**, 7281 (1994).

[44] B. O. Seraphin and N. Bottka, Phys. Rev. **145**, 628 (1966).

[45] D. E. Aspnes, Phys. Rev. **147**, 554 (1966).

[46] R. A. Batchelor, A. C. Brown, and A. Hamnett, Phys. Rev. B **41**, 1401 (1990).

[47] D. E. Aspnes, Surf. Sci. **37**, 418 (1973).

[48] K. Zelazna, M. P. Polak, P. Scharoch, J. Serafinczuk, M. Gladysiewicz, J. Misiewicz, J. Dekoster, and R. Kudrawiec, Appl. Phys. Lett. **106**, 142102 (2015).

[49] M. E. Ziffer, J. C. Mohammed, and D. S. Ginger, ACS Photonics **3**, 1060 (2016).

[50] R. Nedzinskas, B. Cechavicius, J. Kavaliauskas, V. Karpus, G. Valusis, L. H. Li, S. P. Khanna, and E. H. Linfield, Nanoscale Res. Lett. **7**, 609 (2012).

[51] D. E. Aspnes and A. Frova, Solid State Commun. **88**, 1061 (1993).

[52] S. Koeppen and P. Handler, Phys. Rev. **187**, 1182 (1969).

[53] R. R. Lieten, K. Bustillo, T. Smets, E. Simoen, J. W. Ager, III, E. E. Haller, and J.-P. Locquet, Phys. Rev. B **86**, 035204 (2012).

[54] M. Virgilio, C. L. Manganelli, G. Grosso, T. Schroeder, and G. Capellini, J. Appl. Phys. **114**, 243102 (2013).

[55] Y. Cai, Z. Han, X. Wang, R. E. Camacho-Aguilera, L. C. Kimerling, J. Michel, and J. Liu, IEEE J. Sel. Top. Quantum Electron. **19**, 1901009 (2013).

[56] G. Pizzi, M. Virgilio, and G. Grosso, Nanotechnology **21**, 055202 (2010).

[57] V. Sorianello, A. Perna, L. Colace, G. Assanto, H. C. Luan, and L. C. Kimerling, Appl. Phys. Lett. **93**, 111115 (2008).

[58] J. Liu, X. Sun, L. C. Kimerling, and J. Michel, Opt. Lett. **34**, 1738 (2009).

[59] T. H. Cheng, C. Y. Ko, C. Y. Chen, K. L. Peng, G. L. Luo, C. W. Liu, and H. H. Tseng, Appl. Phys. Lett. **96**, 091105 (2010).

[60] G. Grzybowski, R. Roucka, J. Mathews, L. Jiang, R. T. Beeler, J. Kouvetakis, and J. Menéndez, Phys. Rev. B **84**, 205307 (2011).

[61] H. M. van Driel, A. Elci, J. S. Bessey, and M. O. Scully, Solid State Commun. **20**, 837 (1976).

[62] W. Klingenstein and H. Schweizer, Solid State Electron. **21**, 1371 (1978).

[63] S. Manna, A. Katiyar, R. Aluguri, and S. K. Ray, J. Phys. D: Appl. Phys. **48**, 215103 (2015).

[64] Y. Huo, H. Lin, R. Chen, M. Makarova, Y. Rong, M. Li, T. I. Kamins, J. Vuckovic, and J. S. Harris, Appl. Phys. Lett. **98**, 011111 (2011).

[65] J. R. Sanchez-Perez, C. Boztug, F. Chen, F. F. Sudradjat, D. M. Paskiewicz, R. Jacobson, M. G. Lagally, and R. Paiella, Proc. Natl. Acad. Sci. USA **108**, 18893 (2011).

[66] H. Saito, K. Nishi, and S. Sugou, Appl. Phys. Lett. **73**, 2742 (1998).

[67] M. Cardona, K. L. Shaklee, and F. H. Pollak, Phys. Rev. **154**, 696 (1967).

[68] H. R. Philipp and E. A. Taft, Phys. Rev. **113**, 1002 (1959).

[69] R. A. Batchelor and A. Hamnett, J. Appl. Phys. **71**, 2414 (1992).

[70] O. L. Lazarenkova and A. N. Pikhtin, Phys. Status Solidi **175**, 51 (1999).